Cumhuriyet Science Journal
CSJ

e-ISSN: 2587-246X
ISSN: 2587-2680

Cumhuriyet Sci. J., Vol.39-4(2018) 940-953

Structural Characterization of 6-Bromo-5-nitroquinoline-1-oxide: A Quantum Chemical Study and XRD Investigations

Salih ÖKTEN[1*], Cem Cüneyt ERSANLI[2], Osman ÇAKMAK[3]

[1]*Kırıkkale University, Faculty of Education, Department of Maths and Science Education, Division of Science Education, Kırıkkale, TURKEY*

[2]*Sinop University, Faculty of Arts and Science, Department of Physics, Sinop, TURKEY*

[3]*Yıldız Techinical University, Faculty of Arts and Science, Department of Chemistry, İstanbul, TURKEY*

Received: 16.05.2018; Accepted: 08.11.2018 *http://dx.doi.org/10.17776/csj.424045*

Abstract. The chemical properties of recently synthesized 6-bromo-5-nitroquinoline-1-oxide under a mild reaction condition by regioselective nitration of 6-bromoquinoline-1-oxide at C5 on going our research were investigated as theoretical. The crystal structure of 6-bromo-5-nitroquinoline-1-oxide, $C_9H_5BrN_2O_3$, was determined by X-ray analysis. Crystallized in $Pmc2_1$ in the orthorhombic space group with a = 13.6694 (13) Å, b = 9.6036 (10) Å, c = 14.1177 (16) Å, Z = 8, D_x = 1.929 mg/m^3. In this study, theoretical calculations were performed using the GaussView 4.1 molecular imaging program and the Gaussian03W packet program. In the ground state, stable structures of the wholes molecule in the gaseous phase are investigated based on Density Functional Theory (DFT). Molecularly optimized geometries, dipole moments, charge density, thermodynamic properties (heat capacity, enthalpy, entropy), chemical shift values (^{1}H NMR and ^{13}C NMR), energies, molecular electrostatic potentials and frontier orbitals (HOMO and LUMO) B3LYP/6-311G(d,p) base set. Thus, the results obtained by the X-ray diffraction method are supported by theoretical foundations. Finally, the distribution of interactions between molecules in the crystal structure of 6-bromo-5-nitroquinoline-1-oxide (**3**) was investigated by analysis using Hirshfeld surface production and two-dimensional fingerprinting.

***Keywords*:** Nitration, *N*-oxidation, Functionalization, 6-Bromoquinoline-1-oxide, XRD, DFT.

6-Bromo-5-nitrokinolin-1-oksit'in Yapısal Karekterizasyonu: Bir Kuantum Kimyasal Çalışma ve XRD Bulguları

Özet. Devam eden çalışmalarımız kapsamında 6-bromokinolin-1-oksit'in ılıman reaksiyon şartlarında C5 konumundan yerseçici olarak nitrolanmasıyla yakın zamanda sentezlenen 6-bromo-5-nitrokinolin-1-oksit'in kimyasal özellikleri teorik olarak araştırıldı. Bu çalışmaya ilaveten 6-bromo-5-nitrokinolin-1-oksit'in, $C_9H_5BrN_2O_3$, yapısı X-ışınları difraksiyon analizi ile belirlendi. Bu bileşik, elde edilen veriler ile, a=13.6694(13) Å, b=9.6036(10) Å, c=14.1177(16) Å, Z=8, D_x=1.929 mg/m^3, ortorombik kristal yapısında olduğu belirlendi. Bu çalışmada, kuramsal hesaplar GaussView 4.1 molekül görüntüleme programı ve Gaussian03W paket programı kullanılarak yapılmıştır. Temel halde, tüm molekülün gaz fazında yalıtılmış halde bulunan kararlı yapıları, Yoğunluk Fonksiyonel Kuramı (YFT) temel alınarak incelenmiştir. Söz konusu molekülün optimize edilmiş geometrileri, dipol momentleri, yük yoğunluğu, termodinamik özellikler (ısı sığası, entalpi, entropi), kimyasal kayma değerleri (^{1}H NMR and ^{13}C NMR), enerjileri, moleküler elektrostatik potansiyelleri ve öncü orbitalleri (HOMO ve LUMO) B3LYP/6-311G(d,p) baz seti kullanılarak elde edilmiştir. Böylece X-ışını kırınım yöntemi ile elde edilen sonuçlar kuramsal temeller aracılığı ile desteklenmiştir. Son olarak, Hirshfeld yüzey üretimi ve iki boyutlu parmak izi grafikleri kullanılarak yapılan analiz ile bileşiğin kristal yapısındaki moleküllerarası etkileşimleri araştırıldı.

***Anahtar Kelimeler*:** Nitrolama, *N*-oksitleme, İşlevselleştirme, 6-Bromokinolin-1-oksit, X-ışınları difraksiyon, Yoğunluk Fonksiyonel Teori.

* Corresponding author. *Email address:* *sokten@gmail.com; salihokten@kku.edu.tr*

1. INTRODUCTION

Nitrated quinolines are important class of key molecules for synthesizing of amino derivatives for pharmacological use. Moreover antileishmanial [1] and potent mutagenic activities [2] of nitro quinoline *N*-oxide have been reported. The electron-acceptor property of *N* atom in heteroaromatic causes the electron density of *N*-function polycycle aromatics. Thus, possibility of electropfilic substitution in heterocycle of quinoline is very low. Aromatic *N*-oxides contain an oxygen atom bound to a nitrogen atom of the heteroaromatic via a semipolar bond. The *N*-oxide group is a good conductor for introducing a functional group in the position of *ortho* or *para* into the nitrogen atom [3,4]. Also, the *N*-oxide group can demonstrate both electron-donor and electron-acceptor properties depending on the features of the electronic structure of heteroaromatics due to mesomeric structures of *N*-oxide in pyridine cycle [5]. On the other hand, *N*-oxides, routinely used in some reactions, are prototypical oxidants [6]. *N*-oxide form of quinoline has been commonly activated for bromination and nitration reactions at C-2 and C-4 positions. C-2-halogenation via the corresponding *N*-oxides provides an important alternative route because C-2-substituted arenes with *N*-function are common motifs in pharmacological molecules [4]. We have recently explored new synthetic strategy based on bromination of 6,8-disubstituted tetrahydroquinolines (THQs) to give 3-bromo-6,8-disubstituted quinolines [7-9]. Now we plan to synthesize 2- and/or 4-bromo/nitro 6-substituted and / or 6,8-disubstituted quinoline to obtain poly functional quinoline derivatives. For this reason, we are interested in *N*-oxidation and nitration of quinoline. Recently, we have reported the synthesis of bromo *N*-oxide quinoline derivatives were subjected to nitration [10]. First, 6-bromoquinoline (**1**) was treated with *m*-CPBA and converted easily to *N*-oxide form. Then, nitration reaction of 6-bromoquinoline-1-oxide (**2**) was investigated. *N*-oxide form of 6-bromoquinoline (**2**) was transformed to corresponding 4-NO_2 (**4**) and 5-NO_2 (**3**) quinolines by direct nitration reactions, as NH_2 precursor [10]. In this paper, the recently reported quinoline derivative compound, synthesis, crystallographic and quantum chemical computation studies on 6-bromo-5-nitroquinoline-1-oxide are presented here regarding the above phenomenon.

2. MATERIALS AND METHODS

2.1. Synthesis of 6-Bromoquinoline-1-oxide (2)

The synthesis of 6-bromo-5-nitroquinoline-1-oxide (**3**) via bromination reactions with Br_2 and then oxidation reactions with *m*-CPBA were reported recently by our previous publications [8, 10]. The isolated compound (**3**) was fully characterized with melting point, elemental analysis, infrared, ^{1}H, ^{13}C, HMBC and HETCOR spectroscopy in this paper [10]. This study was carried out with 6-bromo-5-nitroquinoline-1-oxide (**3**) according to our previous paper [10].

2.2. Crystal Structure Determination for 6-bromo-5-nitroquinoline-1-oxide (3)

The crystal structure of **3** was evaluated by *Bruker diffractometer* equiped with *APEX-II CCD* detector using graphite monochromated MoK_α radiation and performed at 296 K. A total of 4795 reflections were collected [$2.886^o < \theta < 28.337^o$] and cell parameters were determined using *SAINT* [11]. The crystal structure was determined by intrinsic method *SHELXS-1997* [12] and refined *SHELXL-1997* [12]. All non-hydrogen atomic parameters were anisotropically refined and all H atomic parameters were fixed to 0.93 Å for CH. The U_{iso} values of the H atoms are also fixed to the U_{eq} value of 1.2 times the base atom for CH. Molecular drawings were generated using *ORTEP-III*. CCDC 1525693 contains the supplementary crystal data of **3** for this paper.

2.3. Quantum Chemical Calculation for Compound 3

The Gaussian03W [13] software package was used for all quantum chemical calculations. The compound **3** was optimized at DFT(B3LYP) method with the 6-311G(d,p) basis set using the

GaussView 4.1 interface program [14] in the gaseous phase. For modeling, formation of **3** was first obtained from X-ray coordinates. Optimized geometrical structures and the net charges of Mulliken were investigated using DFT (B3LYP) method with 6-311G(d,p) basic set. The solvent phase calculations have been employed with IPCM (Polarized Continuum Model (PCM) with Isodensity version) [15] in the three solvent enviroments with ε = 4.711, ε = 24.852, ε = 78.355 to simulate chloroform, ethanol, water, respectively. The highest occupied molecular orbital (E_{HOMO}) and lowest molecular orbital (E_{LUMO}) analysis was performed to account for the transfer of charge within the molecule. The chemical hardness (η), chemical softness (σ), electronegativity (χ), electronic chemical potential (μ), electron affinity (A), ionization potential (I), energy gap (ΔE) were calculated using HOMO and LUMO. Dipole moment (μ), linear polarization (α) and initial hyperpolarisability (β) were also calculated. ^{1}H and ^{13}C NMR isotropic protection values were calculated by Gauge Including Atomic Orbital method [16], using optimized geometry using the B3LYP level. Molecular electrostatic potential (MEP) was assessed using the B3LYP/6-311G(d,p) method to investigate the reactive sites of compound **3**. The thermodynamic parameters of compound **3** were determined to study entropy, heat capacity and enthalpy change, their dependence on temperature at temperatures ranging from 100K to 800K. Finally, the distribution of interactions between molecules in the compound **3** was investigated by analysis using Hirshfeld surface production and two-dimensional fingerprinting.

3. RESULTS AND DISCUSSION

3.1. Synthesis

In order to facilitate the nitration at the pyridine ring of quinoline moiety, we have recently reported that *N*-oxidation of 6-bromoquinoline was tried with an oxidizing agents. The *N*-oxidation was carried out with *m*-CPBA (Fig. 1). The *N*-oxidation of 6-bromoquinoline (**1**) occurs smoothly to give compound (**2**) with *m*-CPBA in yield of 87% (Fig. 1).

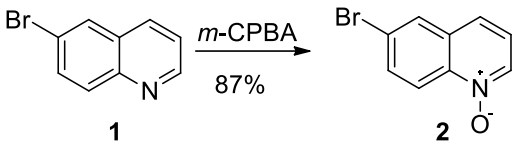

Figure 1. *N*-oxidation of 6-bromoquinoline (**1**).

Then, quinoline *N*-oxide (**2**) was subjected to nitrate. For this purpose, into the crushred ice 6-bromoquinoline-1-oxide (**2**) was added slowly nitration reactant (HNO_3/H_2SO_4) [10]. After completing the reaction (by stirring 4h) classical working up procedure gave a product mixture. The mixture of products, 6-bromo-5-nitroquinoline-1-oxide (**3**) and 4-nitro-6-bromoquinoline-1-oxide (**2**), were isolated by column chromatography in yields of 57% and 29%, respectively (Fig. 2) [10].

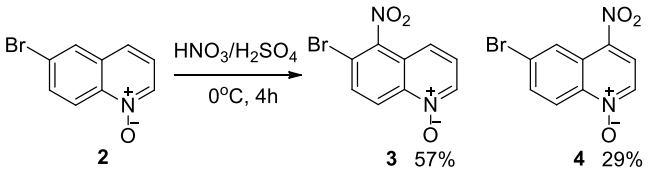

Figure 2. Nitration of 6-bromoquinoline-1-oxide (**2**).

3.2. X-ray Crystal Structure

6-Bromo-5-nitroquinoline-1-oxide (**3**) contains three molecules (I-III) in the asymmetric unit (Fig. 3, Table 1).

Table 1. The selected crystal data and structure refinement parameters for **3**.

Empirical formula	$C_9H_5BrN_2O_3$
Formula weight	269.06
Crystal system	orthorhombic
Space group	$Pmc2_1$
a (Å)	13.6694(13)
b (Å)	9.6036(10)
c (Å)	14.1177(16)
V (Å^3)	1853.3(3)
Z	8
D_c (g cm^{-3})	1.929
μ (mm^{-1})	4.422
θ range (º)	2.886-28.337
Measured refls.	78841
Independent refls.	4108
R_{int}	0.0464
S	1.221
$R1/wR2$	0.0448/0.0751
$\Delta\rho_{max}/\Delta\rho_{min}$ (eÅ^{-3})	0.624/-0.737

The selected bond lengths, and angles of **3** are given in Table 2. The dihedral angle between pyridine rings (C1-C4/C9/N1 and C19-C22/C27/N5) and phenyl rings (C4-C9 and C22-C27) for (I) and (III) are 0°. The dihedral angle between pyridine ring [(C10-C13/C18/N3) with a maximum deviation of 0.0062(1) Å for C18] and phenyl ring [(C13-C18) with a maximum deviation of 0.0068(1) Å for C16] is 0.80° for (II). The C-N, C-Br and N-O bond distances [1.315(13), 1.488(11), 1.861(9), 1.277(10) and 1.197(6) Å for (I), 1.330(10), 1.480(8), 1.889(7), 1.310(8) and 1.213(8) Å for (II), and 1.325(12), 1.482(11), 1.898(8), 1.299(10) and 1.167(7) Å for (III), respectively] are the most sensitive indicators of the compound **3**. In crystal **3**, interactions of C-H...Br and C-H...O are observed (Table 3).

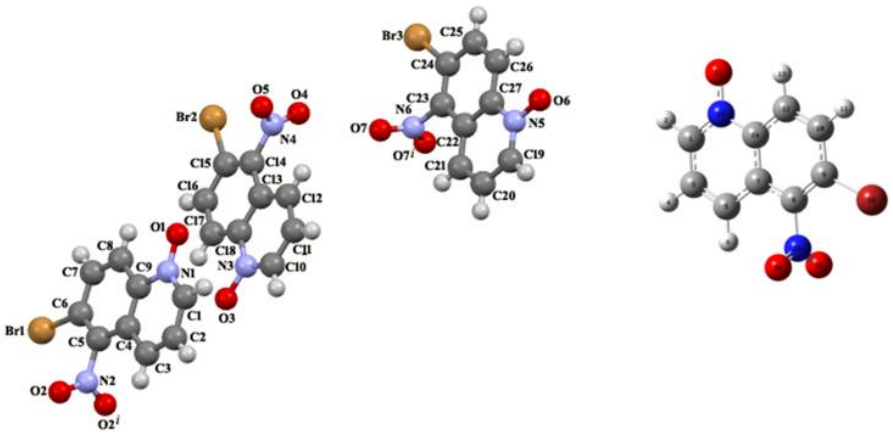

(a) **(b)**

Figure 3. (a) *ORTEP-III* diagram, **(b)** Optimized geometry of compound **3**.

Table 2. In the case of ground, optimized (DFT/B3LYP-gaseous phase) with the level of 6-311G(d,p) and experimental geometries of compound **3**.

	X-ray	DFT/B3LYP		X-ray
Bond lengths (Å)			*Bond lengths* (Å)	
C1-N1	1.315(13)	1.352	C18-N3	1.404(8)
C5-N2	1.488(11)	1.489	N3-O3	1.310(8)
C6-Br1	1.861(9)	1.903	N4-O4	1.213(8)
C9-N1	1.425(13)	1.426	N4-O5	1.206(8)
N1-O1	1.277(10)	1.278	C19-N5	1.325(12)
N2-O2	1.197(6)	1.219	C27-N5	1.404(11)
N2-O2	1.197(6)	1.219	C24-Br3	1.898(8)
C10-N3	1.330(10)		C23-N6	1.482(11)
C14-N4	1.480(8)		N5-O6	1.299(10)
C15-Br2	1.889(7)		N6-O7	1.167(7)
Bond angle (°)			*Bond angle* (°)	
N1-C1-C2	122.9(10)	123.7	O4-N4-O4	117.6(7)
O1-N1-C1	122.7(8)	121.5	C15-C14-N4	119.3(7)
O1-N1-C9	119.5(8)	119.7	C13-C14-N4	117.6(7)
C1-N1-C9	117.8(8)	118.7	C14-C15-Br2	121.7(5)
C6-C5-N2	118.8(9)	120.8	C16-C15-Br2	118.3(5)
C4-C5-N2	115.8(9)	116.8	C17-C18-N3	119.5(6)
C5-C6-Br1	123.5(7)	124.2	N5-C19-C20	121.4(8)
C7-C6-Br1	119.5(7)	119.8	O6-N5-C19	121.3(7)
C8-C9-N1	117.9(9)	118.3	O6-N5-C27	118.8(8)
C4-C9-N1	120.1(8)	120.5	C24-C23-N6	119.6(8)
N3-C10-C11	121.9(7)		C23-C24-N6	118.4(8)
O2-N2-C5	118.2(4)	116.7	C23-C24-Br3	120.1(8)
O3-N3-C10	121.7(6)		C25-C24-Br3	119.3(7)
O3-N3-C18	118.0(6)		C22-C27-N5	119.3(8)
O5-N4-O4	124.7(7)		C26-C27-N5	118.5(8)
Torsion angles (°)			*Torsion angles* (°)	
C2-C1-N1-O1	180.0(2)	180.0	C14-C13-C18-N3	-179.8(6)
N2-O2-C5-C6	-90.2(8)°	-90.6		
N4-C14-C15-C16	-178.4(7)		C17-C18-N3-O3	-0.3(10)

Table 3. The parameters of C-H...Br and C-H...O interactions (Å, º) for **3**.

D–H···A	D–H	H···A	D···A	D–H···A
C8-H8…Br1^{i}	0.93	2.74	3.665(9)	171.2
C17-H17…Br2^{ii}	0.93	2.80	3.708(7)	166.3
C25-H25…O7^{i}	0.93	2.52	3.376(11)	153.9
C25-H25…O7^{iii}	0.93	2.52	3.376(11)	153.9

Symmetry codes: (*i*) -*x*+1, -*y*+2, *z*+1/2, (*ii*) *x*, -*y*+2, *z*-1/2, (*iii*) *x*+2, -*y*+1, *z*+1/2

3.3. Optimized Molecular Structure

The optimized molecular structure (Fig. 3) of the selected theoretical inters atomic bond lengths, and angles are compared with the experimental parameters obtained by X-ray analysis and the results are shown in Table 2. The values were estimated considering some bond lengths in Table 2 are slightly longer than the experimental ones. These differences are caused by a solid phase belonging to the experimental results; theoretical calculation belongs to the gaseous phase. The result of the different parameters of binding between the calculated and experimental values, together with the intermolecular interactions of the molecules due to the presence of the crystalline solid state area is due to the interaction with each other [17]. In the structure, the orientation of the nitro phenyl ring of compound **3** is defined by the torsion angle N2-O2-C5-C6 = -90.2(8)° for B3LYP/6-311G(d,p) level (calculated at -90.6°). As can be seen from Table 2, the difference between X-ray and calculated values for C1-N1, C5-N2 and C6-Br1 bond lengths is 0.037 Å, 0.001 Å and 0.042 Å, respectively. Similarly, the difference for the N1-C1-C2, C5-C6-Br1 and C8-C9-N1 bond angles is 0.8º, 0.7º and 0.4º, respectively. This small difference is due to the interactions of hydrogen bonds between molecules. A logical method for global comparison of the theoretical calculations is to overlay the molecular skeleton obtained from X-ray diffraction with an RMSE of 0.024 Å for the calculation of DFT/6-311G(d,p) (Fig. 4). The size of the RMSE can be explained by the absence of coulombic interaction between neighboring molecules in the gaseous phase and the results of the experiment correspond to the interactive molecule in the crystal lattice.

Figure 4. Atom-atom superposition of (red) structure calculated on X-ray structure (blue) for compound 3.

3.4. Non linear Optical (NLO) Properties and Dipole Moment

Some of the nitro substitute pyridine materials show efficient NLO properties that can be used in various NLO devices. High values of dipole moment, polarization and hyperpolarization are known to be important for more active NLO properties. In this work, the calculation of the total molecular dipole moment (μ_{total}), linear polarization (α_{total}) and first degree hyperpolarization (β_{total}) from the Gaussian output is explained in detail and DFT is widely used as an effective method for investigating organic NLO materials [18]. The dipole reflects the molecular charge distribution in three directions that can be used to describe the charge motion in the momentum of the molecule. Using the μ, the α_{total}, β, and the *x*, *y*, and *z* components, β_{vec} is defined as:

$$\mu=\sqrt{\mu_x^2+\mu_y^2+\mu_z^2} \quad (1)$$

$$\alpha=\frac{\alpha_{xx}+\alpha_{yy}+\alpha_{zz}}{3} \quad (2)$$

$$\beta=\sqrt{(\beta_{xxx}+\beta_{xyy}+\beta_{xzz})^2+(\beta_{yyy}+\beta_{xxy}+\beta_{yzz})^2+(\beta_{zzz}+\beta_{xxz}+\beta_{yyz})^2} \quad (3)$$

$$\beta_{vec}=\frac{3}{5}\left[\left(\beta_x^{\,2}+\beta_y^{\,2}+\beta_z^{\,2}\right)^{1/2}\right] \quad (4)$$

From Table 4, the calculated total dipole moment, μ_{total}, is equal to 1.3017 D, the highest value among the components is equal to -1.0703 D and μ_x in the x direction. The calculated polarizability of **3** is calculated as 18.024156x10^{-24} esu. Theoretically, the urea, calculated μ_{total}, α_{total} and β_{total} values are 3.6209 D, 4.1495×10^{-24} esu, 0.6059×10^{-30} esu using DFT/B3LYP/6-311G(d,p) method. The μ_{total} value is smaller; a total value of **3** is higher than the urea molecule. The α_{total} value of **3** is 4.3437 times higher than the urea value. It can be observed that the calculated **3** values are 3.5612x10^{-30}esu and about 5.8776 times more than the urea value. The high β value is responsible for the second order NLO properties. For this reason, value suggests the possibility of technological applications.

Table 4. The dipole moment (D), linear polarizability (esu), first hyperpolarizability components and β_{total} value (esu) for gaseous phase in **3**.

	B3LYP/6-311G(d,p)		B3LYP/6-311G(d,p)
μ_x	-1.0703	β_{xxx}	-3.1949x10^{-30}
μ_y	-0.7404	β_{xxy}	-1.3479x10^{-30}
μ_z	0	β_{xyy}	0.0646x10^{-30}
μ_{total}	1.3017	β_{yyy}	-0.1636x10^{-30}
		β_{xxz}	-0.0093x10^{-30}
α_{xx}	29.849032x10^{-24}	β_{xyz}	-0.0079x10^{-30}
α_{xy}	2.9654057x10^{-24}	β_{yyz}	-0.0037x10^{-30}
α_{yy}	24.223344x10^{-24}	β_{xzz}	-0.0859x10^{-30}
α_{xz}	-0.000035x10^{-24}	β_{yzz}	-0.0190x10^{-30}
α_{yz}	-0.000005x10^{-24}	β_{zzz}	0
α_{zz}	10.017557x10^{-24}	β_{total}	3.5612x10^{-30}
α_{total}	18.024156x10^{-24}	β_{vec}	2.1367x10^{-30}

3.5. HOMO-LUMO Analysis

Properties such as molecular orbitals and energy are very useful for quantum chemistry for chemists and physicists. Frontier molecular orbitals are important in determining molecular reactivity and the ability of the molecule to absorb light. It is also important for optical and electrical properties. The HOMO and LUMO are the basic orbitals involved in the chemical reaction. The HOMO energy defines electron donation, the LUMO energy defines electron acceptance, and the difference between HOMO LUMO defines molecular chemical stability [19]. The energy difference between HOMO and LUMO was calculated as 2.924 eV. As can be from Fig. 5, the LUMO is placed on the NO_2 group attached to the phenyl ring, while the HOMO localized on the groups exluding NO_2 group, Br1, C3, C4-C9 and hydrogen atoms.

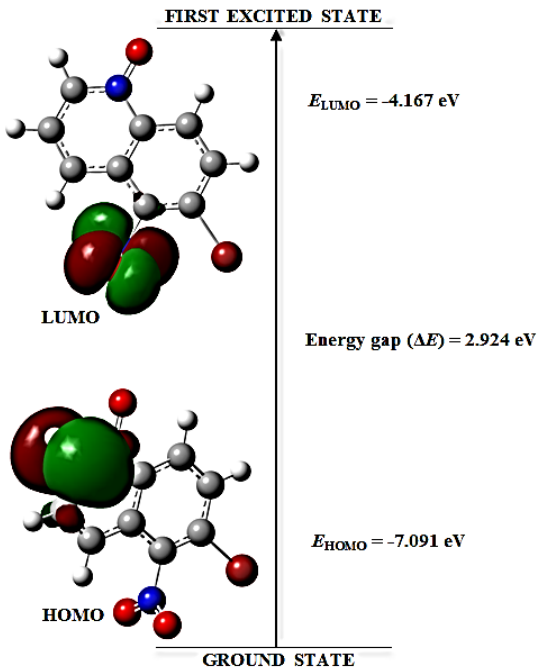

Figure 5. The representation of HOMO and LUMO of 3.

The E_{total}, E_{HOMO}, E_{LUMO}, ΔE, A, I, η [$(I-A)/2$], χ [$(I+A)/2$], μ [$-\chi$], and S [$1/2\eta$] were calculated by PCM using B3LYP/6-311G(d,p) level in gaseous and three solvent phase [20]. The results are listed in Table 5. However, we can conclude that the η and the ΔE decrease with the increasing polarity of the solvent, while the S and the χ increase with increasing polarity of the solvent for the compound 3. The higher the polarization of the solution, the less the chemical stability of the molecule.

Table 5. The energies calculated for three different solvents, frontier orbital energies, chemical hardness and dipole moments.

	DFT/B3LYP with 6-311G(d,p)			
	Gaseous phase	Chloroform	Ethanol	Water
E_{total} (Hartree)	-3255.2887898	-3255.2967137	-3255.2994243	-3255.2999127
E_{HOMO} (eV)	-7.091	-7.157	-7.198	-7.206
E_{LUMO} (eV)	-4.167	-4.290	-4.332	-4.341
ΔE (eV)	2.924	2.867	2.866	2.865
A=- E_{LUMO} (eV)	4.167	4.290	4.332	4.341
I=- E_{HOMO} (eV)	7.091	7.157	7.198	7.206
η=(I-A)/2 (eV)	1.462	1.434	1.433	1.432
χ = (I+A)/2 (eV)	5.629	5.724	5.765	5.774
S =1/2η (eV)$^{-1}$	0.342	0.349	0.349	0.349
μ = - χ (eV)	-5.629	-5.724	-5.765	-5.774
μ (D)	1.301	1.457	1.511	1.522

3.6. Atomic Charges

Atomic charges in the molecule are essential for chemistry. Mulliken atomic charges were calculated using the B3LYP/6-311G(d,p) method and summarized in Table 6. It is important to note that compound **3** has positive charges of atoms Br1, N2, C1, C3, C5, C8 and C9. The other C and O atoms and N1 exhibit negative charges. All H atoms exhibit a net positive charge. The most positively charged atoms were found to be C5 and N2. For this reason, it may be attributed to a larger ionic character (N2-O2).

Table 6. Calculated net charges by Mulliken population method for the compound **3**.

Atoms	Atomic charges	Atoms	Atomic charges
Br1	0.070045	C5	0.140548
N1	-0.134746	C6	-0.120889
N2	0.124498	C7	-0.013432
O1	-0.389788	C8	0.049993
O2	-0.237795	C9	0.183235
O2	-0.237795	H1	0.112636
C1	0.188064	H2	0.101796
C2	-0.198222	H3	0.082592
C3	0.159248	H7	0.109002
C4	-0.107294	H8	0.118306

3.7. ^{1}H and ^{13}C NMR Spectra

The combination use of nuclear magnetic resonance (NMR) technology and computational methods provides a strong approach to achieving more accurate results. The NMR values were obtained using the B3LYP method for the optimized $C_9H_5BrN_2O_3$ molecule. The atomic orbital method was used to calculate the NMR value of the molecule. Calculations of NMR spectra were performed for the chloroform solvent. The isotropic protection values were used to calculate isotropic chemical changes according to tetramethylsilana. The experimental results [10] and theoretical results obtained in ^{1}H and ^{13}C NMR spectra are presented in Table 7. Given that the chemical exchange range of ^{13}C NMR for a typical organic molecule is > 100 ppm [21] in general, accuracy provides reliable interpretation of spectroscopic parameters. In this study, it is expected that ^{13}C NMR chemical shifts in the ring will be > 100 ppm. Experimental and theoretical chemical shifts of compound **3** range between 115.2-147.9 and 115.09-149.13 ppm, respectively. The calculated ^{13}C NMR chemical shift value of the C5 bound to the Nitro group is slightly higher than the ring carbon atoms that peak at 147.9 when calculated at 149.13 ppm.

Table 7. Experimental and theoretical ^{1}H and ^{13}C NMR isotropic chemical shift values of the molecule.

Atoms	Experimental	Theoretical	Atoms	Experimental	Theoretical
C2	136.6	138.54	H2	8.58	8.54
C3	123.5	124.98	H3	7.46	7.49
C4	115.2	115.09	H4	7.54	7.52
C5	147.9	149.13	H7	7.96	7.82
C6	124.3	123.82	H8	8.79	8.81
C7	133.7	133.31			
C8	118.6	119.71			
C9	140.6	141.01			
C10	124.2	126.86			

The ^{1}H NMR chemical shifts of the hydrogen atoms bonded to the pyridine ring were observed between 8.58 and 7.46 ppm. These signals were also calculated at 8.54 and 7.49 ppm using the B3LYP level. The ^{1}H NMR peaks for the H7 and H8 atoms observed at 7.96 and 8.79 ppm were 7.82 and 8.80 ppm, respectively. The relationships between experimental and calculated chemical shifts (δ) are explained by the following equation:

$$\delta_{cal.}\ (ppm) = 1.00748\ \delta_{exp.} - 0.09366\ (R^2 = 0.9999) \quad (5)$$

The correlation between the calculated and experimental chemical shifts was obtained and Fig. 6 shows the change in this correlation.

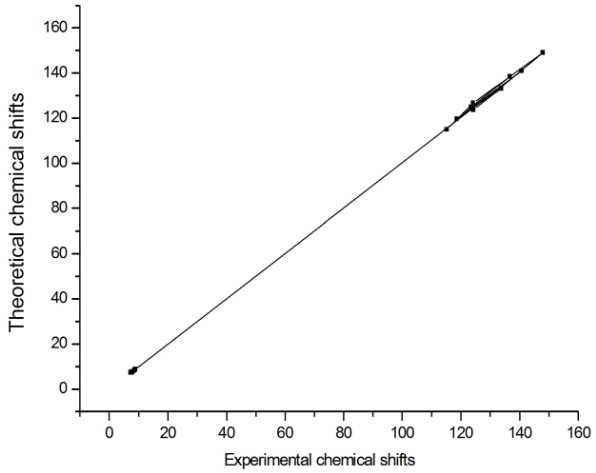

Figure 6. Correlation graph of the theoretical and experimental NMR spectrum of compound **3**.

3.8. Molecular Electrostatic Potential

MEP, which is a graph of electron density and electrostatic potential is mapped onto a hard surface. MEP was used primarily to predict hydrogen bond interactions and biological reactivity and reactivity to electrophilic attack. While red and yellow regions on the MEP map are associated with higher electron density, light blue and blue regions on the MEP map are associated with lower electron density. Figure 5 shows the MEP map representing a potential distribution in the range -0.04504 a.u. and 0.03785 a.u.. Negative electrostatic potential values are mainly on the NO_2 group, which is mainly bound to oxygen, while there is a positive electrostatic potential, especially around the oxygen atoms (H1, H2, H7 and H8 atoms). At the same time, these regions indicate the nucleophilic and electrophilic attack of **3**. We can also use MEP analysis knowledge to predict whether hydrogen bonds between molecules and between molecules are present between atoms. In addition, the results of the the crystal structure **3** analyzes provide supportive information on the MEP map. So, as mentioned above, the compound is C25-H25... $O7^i$ between two molecules, namely C-H... O type, between the oxygen atom and phenyl of the nitro part. It can be said that the interaction between C-H...O type molecules of Fig. 7 and also this region in the studied structure reflects character electron donor.

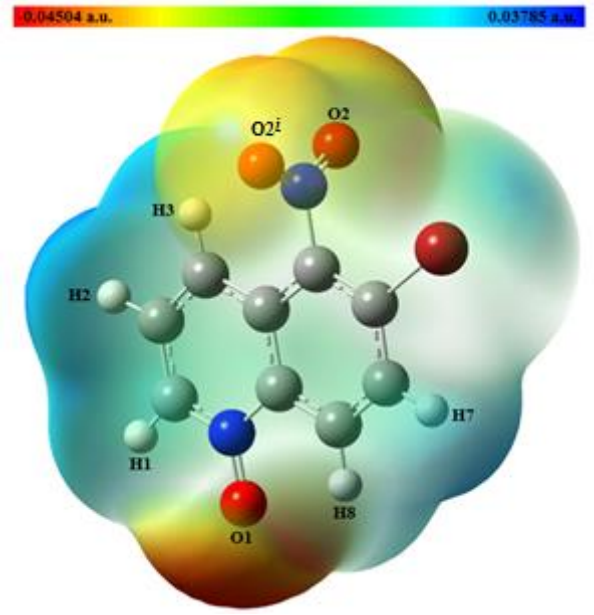

Figure 7. MEP map of mentioned compound **3** at B3LYP method in gaseous phase.

3.9. Thermodynamic Properties

Some thermodynamic parameters are presented in Table 8 using the B3LYP/6-311G(d,p) method in the ground state. As shown in Table 8, enthalpy, standard heat capacity and entropy increase from 100 to 800 K, because molecular vibrations increase with increasing temperature. The correlation equations between heat capacity ($C^o_{p,m}$), entropy (S^o_m), enthalpy (H^o_m) and temperatures are equipped with quadratic formulas, and the corresponding fiting regression coefficients for these thermodynamic properties (R^2) are 0.99958, 0.99998, and 0.99966 respectively (Eqs. 6-8), the following and Correlation graphs are shown in Fig. 8.

$$C^o_{p,m} = 0.48083 + 0.16736\ T - 8.00859 \times 10^{-5}\ T^2 \quad (R^2 = 0.99958) \tag{6}$$

$$S^o_m = 56.80129 + 0.18041\ T - 4.73622 \times 10^{-5}\ T^2 \quad (R^2 = 0.99998) \tag{7}$$

$$H^o_m = -1.08469 + 0.01577\ T + 4.81226 \times 10^{-5}\ T^2 \quad (R^2 = 0.99966) \tag{8}$$

All thermodynamic data provides useful information about quinoline for further study. They can be used to calculate other thermodynamic energies according to the relationships of thermodynamic functions and predict the aspects of chemical reactions according to the second law of thermodynamics.

Table 8. Thermodynamic parameters for compound **3**.

Temperature (K)	$C^o_{p,m}$ (Cal mol^{-1} K^{-1})	S^o_m (Cal mol^{-1} K^{-1})	H^o_m (k Cal mol^{-1})
100	17.071	74.178	1.268
200	29.901	91.264	3.806
298.15	42.842	106.427	7.576
400	54.889	121.333	12.772
500	64.575	135.106	18.962
600	72.220	147.946	26.016
700	78.229	159.854	33.749
800	83.003	170.889	42.018

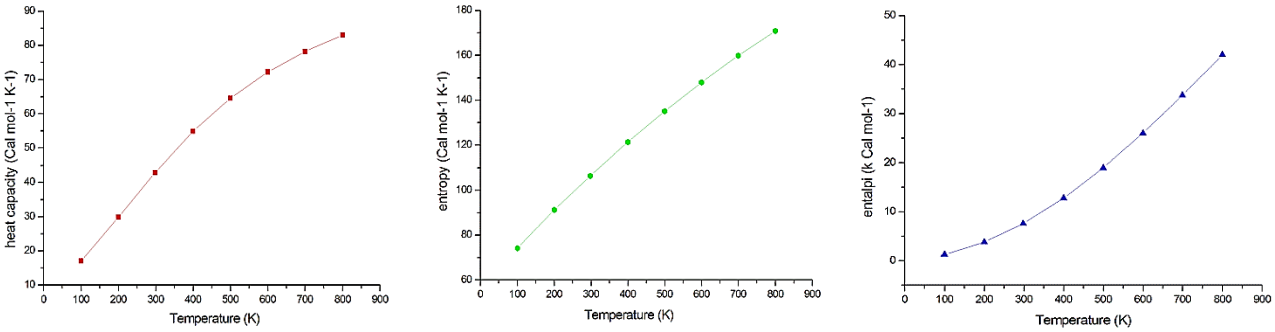

(a) (b) (c)

Figure 8. Correlation graphics of **3**.

3.10. Hirshfeld Surface Analysis

Hirshfeld surfaces and fingerprint charts were created for the compound based on the crystalographic information file (CIF) using CrystalExplorer [22]. The Hirshfeld surfaces mapped with their composition, d_{norm}, shape index and curvedness functions are shown in Fig. 9. In Fig. 9, (-0.2019) and (+1.1929) Å show the surfaces mapped on d_{norm} with constant color scale. The d_{norm} surface is used to define close inter-intermolecular interactions, and the surface is mapped in the red-blue-white color scheme. The Red zones represent contacts closer to the Van der Waals radius, the blue zones are longer than the van der Waals radius, and the white zones represent equal distance of contact to the Van der Waals separation. Shape index and curvedness surfaces are mostly used for packaging modes, planar stacking arrangements and the contact of neighboring molecules with each other [22]. Fig. 10 show the Hirshfeld surfaces mapped over d_i (0.9695 to 2.6378 Å), d_e (0.9707 to 2.6785 Å), shape index (-1.0 to 1.0 a.u.), fragment patch (-0.0 to 13.0 a.u.), and curvedness (-4.0 to 0.4 a.u.).

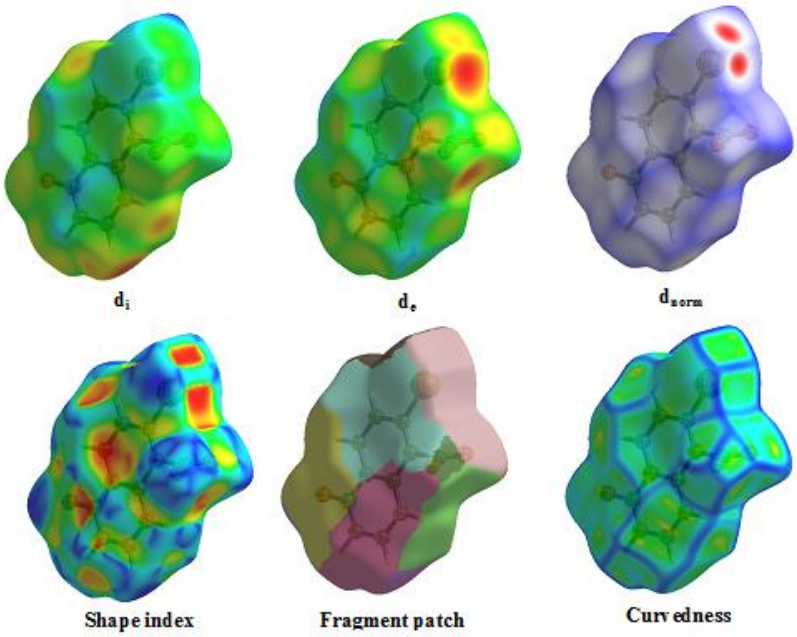

Figure 9. Hirshfeld surfaces mapped with d_i, d_e, d_{norm}, fragment patch, curvedness and shape index functions of **3**.

Table 9. Summary of short interatomic contacts (Å) in compound **3**.

Contact	*Distance*	Symmetry operation
Br2.....H17	2.80	*x, -y+2, x-1/2*
Br2.....H11	2.99	*x, +y-1, +z*
O4... ..H10	2.69	*x, -y+1, +z-1/2*
298.15		

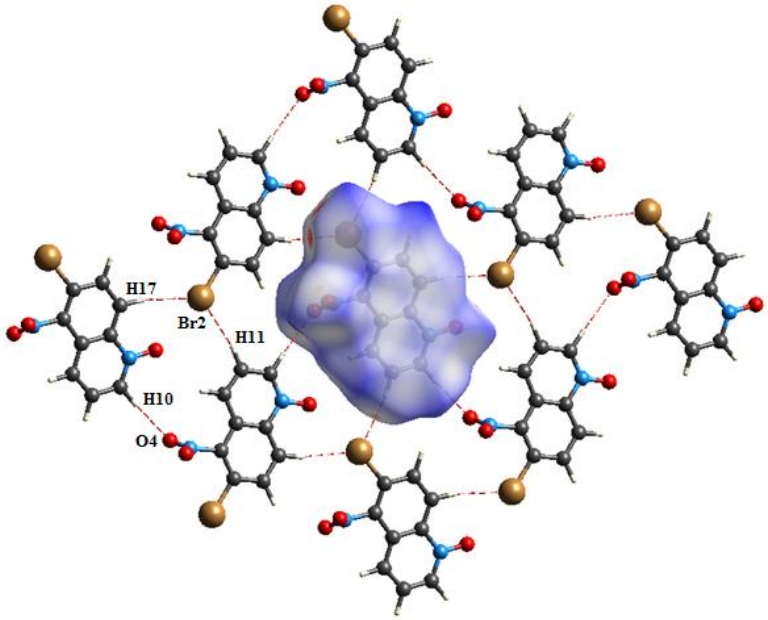

Figure 10. View of 3D Hirshfeld surface of **3** mapped over d_{norm}.

Fig. 11 shows a 2D fingerprint graph and disaggregated fingerprint plots containing all intermolecular interactions of the Hirschfeld surface. 2D fingerprint graphics particularly demonstrate the presence of the interaction O…H and Br…H in the compound **3**. In the compound **3**; the presence of O…H/H…O, H…Br/Br…H, H…H, H…C/C…H, C…C, C…O/O…C, C…Br/Br…C, O…Br/Br…O, O…O, O…N/N…O, C…N/N…C, H…N/N…H, Br…Br and N…N interactions was observed and the contributions to total Hirshfeld surfaces were 35.3%, 13.9%, 10.3%, 8.9%, 6.4%, 6.1%, 5.6%, 5.3%, 3.5%, 1.9%, 1.6%, 0.5%, 0.4% and 0.3%, respectively.

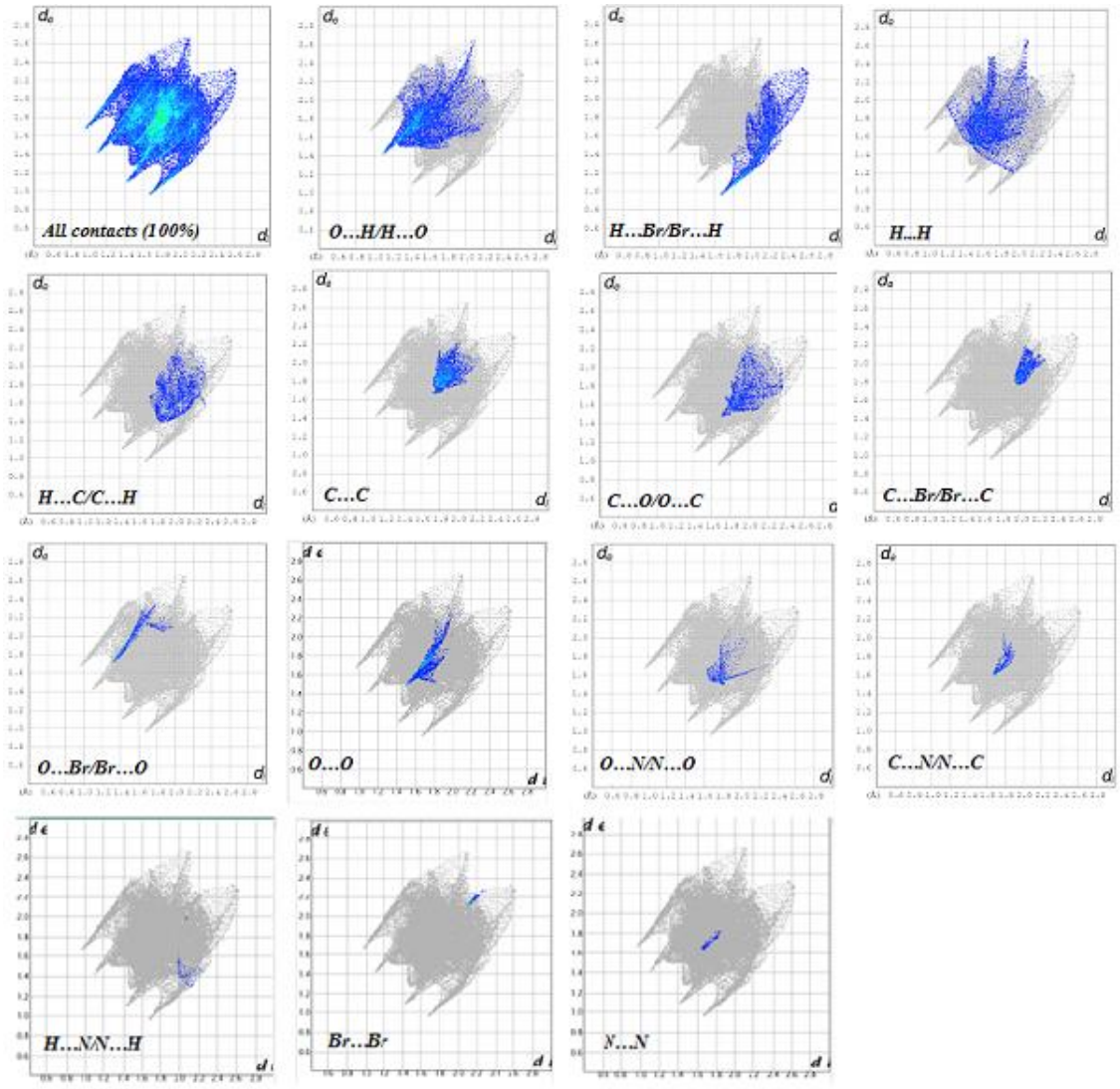

Figure 11. 2D fingerprint graph and disaggregated fingerprint graphs containing all intermolecular interactions of the compound **3**.

4. CONCLUSION

6-Bromo-5-nitroquinoline-1-oxide was characterized by X-ray crystallographic technique. Theoretical calculations were performed based on the DFT/6-311G(d,p) set. The geometric parameters of the compound, NMR chemical shifts and Mulliken population analyzes were theoretically determined. The obtained data were compared with experimental values. In the study, the experimental data are obtained in the solid phase, whereas the theoretical data are obtained in

the gaseous phase. However, the results obtained for the structure in general have been determined by us to be compatible with each other. The most positively charged atoms were found to be C5 and N2. For this reason, it may be attributed to a larger ionic character (N2-O2). HOMO, LUMO, MEP and thermodynamic analyzes were performed to obtain information on electrophilic and nucleophilic characteristic properties. Furthermore, the NLO analysis was obtained using a theory at the same level and the α_{total} and β_{total} values of **3** are 4.3437 and 5.8776 times higher than the urea value. Thus, compound **3** may be a good candidate for NLO material and applications. As a result of the Hirshfeld surface analysis, O…H and Br…H contacts played an important role in the crystal packaging stability of 6-bromo-5-nitrochinolin-1 oxide. We hope that all of these results will create an infrastructure for research that performs other quinoline derivatives or that similar studies can be used for further analysis.

Acknowledgements

This study was supported by grants from the TÜBİTAK (project no: 112T394). The authors acknowledge Scientific and Technological Research Application and Research Center, Sinop University, Turkey, for the use of the Bruker D8-QUEST diffractometer.

REFERENCES

[1] Paloque L., Verhaeghe P., Casanova M., Castera-Ducros C., Dumètre A., Mbatchi L., Hutter S., Kraiem-Mrabet M., Laget M., Remusat V., Rault S., Rathelot P., Azas N. and Vanelle P., Discovery of A New Antileishmanial Hit in 8-Nitroquinoline Series, Eur. J. Med. Chem., 54 (2012) 75-86.

[2] Nunoshiba T. and Demple B., Potent Intracellular Oxidative Stress Exerted by the Carcinogen 4-Nitroquinoline-*N*-oxide, Cancer Res., 53-14 (1993) 3250-3252.

[3] Wu J., Cui X., Chen L., Jiang G.and Wu Y., Palladium-Catalyzed Alkenylation of Quinoline-*N*-oxides via C-H Activation under External-Oxidant-Free Conditions, J. Am. Chem. Soc., 131 (2009) 13888-13889.

[4] Wengryniuk S.E., Weickgenannt A., Reiher C., Strotman N.A., Chen K., Eastgate M.D. and Baran P.S., Regioselective Bromination of Fused Heterocyclic *N*-Oxides, Org. Lett., 15-4 (2013) 792-795.

[5] Romanov V.V., Nizhnik Y.P. and Fofanov A.D., Conformational and Structural Analysis of Bis(4-chloroquinoline-*N*-oxide)hydrogen Tribromide, J. Struct. Chem., 56-2 (2015) 365-369.

[6] Pool J., Scott B. and Kiplinger J.A., A New Mode of Reactivity for Pyridine *N*-Oxide: C-H Activation with Uranium (IV) and Thorium (IV) Bis(alkyl) Complexes, J. Am. Chem. Soc., 127-5 (2005) 1338-1339.

[7] Çakmak O. and Ökten S., Regioselective Bromination: Synthesis of Brominated Methoxyquinolines, Tetrahedron, 73-36 (2017) 5389-5396.

[8] Ökten S., Eyigün D. and Çakmak O., Synthesis of Brominated Quinolines, Sigma J. Eng. Nat. Sci., 33 (2015) 8-15

[9] Ökten S. and Çakmak O., Synthesis of Novel Cyano Quinoline Derivatives, Tetrahedron Lett., 56-39 (2015) 5337-5340.

[10] Çakmak O., Ökten S., Alımlı D., Saddiqa A. and Ersanlı C.C., Activation of 6-Bromoquinoline by Nitration and *N*-oxidation: Synthesis of Substituted Quinolines, Arkivoc, iii, (2018) 362-374.

[11] APEX-II, SAINT and SADABS; Bruker AXS Inc.: Madison, WI, 2014.

[12] Sheldrick G.M., SHELXS-97 and SHELXL-97, Program for Solution Crystal Structure and Refinement, University of Göttingen, Göttingen, 1997.

[13] Frisch A., Nielsen A.B. and Holder A.J., GaussView Users Manual, Gaussian Inc., Pittsburgh, PA., 2001.

[14] Dennington R.I., Keith T., Millam J., Eppinnett K. and Hovell W., GaussView Version 4.1, 2003.

[15] Miertus S., Scrocco E. and Tomasi J., Electrostatic Interaction of a Solute with a Continuum. A Direct Utilizaion of *ab-initio* Molecular Potentials for The Prevision of Solvent Effects, Chem. Phys., 74 (1981) 117-129.

[16] London F., Quantum Theory of Interatomic Currents in Aromatic Compounds. J. Phys. Radium, 8 (1937) 397-409.

[17] Tanak H., Crystal Structure, Spectroscopy, and Quantum Chemical Studies of (*E*)-2-[(2-Chlorophenyl)iminomethyl]-4-trifluoromethoxyphenol J. Phys. Chem. A, 115 (2011) 13865-13876

[18] Babu G.A. and Ramasamy P., Growth and characterization of an organic NLO material ammonium malate, Current Appl. Phys., 10-1 (2010) 214-220.

[19] Fukui K., Role of Frontier Orbitals in Chemical Reactions, Science, 218 (1982) 747-754.

[20] Parr R.G. and Chattaraj P.K., Principle of Maximum Hardness, J. Am. Chem. Soc., 113-5 (1991) 1854-1855.

[21] Kalinowski H.O., Berger S. and Braun S., Carbon-13 NMR Spectroscopy, 4th ed. Chichester: John Wiley & Sons, 1988; pp 512-543.

[22] Spackman M.A. and Jayatilaka D., Hirshfeld Surface Analysis, Crystal engineering communications, 11 (2009) 19-32.